SUPPLEMENTAL MATERIALS

Intercellular Conduction Optimizes Arterial Network Function and Conserves Blood Flow Homeostasis during Cerebrovascular Challenges

Anil Zechariah PhD[1], Cam Ha T. Tran PhD[2,3], Bjorn O. Hald PhD[4] Shaun L. Sandow PhD[5], Maria Sancho PhD[1], Michelle Sun Mi Kim MSc[1], Sergio Fabris PhD[1], Ursula I. Tuor PhD[2], Grant R.J.Gordon PhD[2] and Donald G. Welsh PhD[1, 2]

[1]Robarts Research Institute and the Department of Physiology and Pharmacology, University of Western Ontario, London, Ontario, Canada N6A 5B7

[2]Hotchkiss Brain Institute, Libin Cardiovascular Institute and the Department of Physiology and Pharmacology, University of Calgary, Calgary, Alberta, Canada T2N 4N1

[3]Department of Physiology and Cell Biology, University of Nevada, Reno, Nevada, USA 89557

[4]Department of Neuroscience, Translational Neurobiology, University of Copenhagen, Blegdamsvej 3, DK-2200 Copenhagen N, Denmark

[5]University of the Sunshine Coast, Locked Bag 4, Maroochydore DC, Queensland 4558 Australia

Supplemental Figures

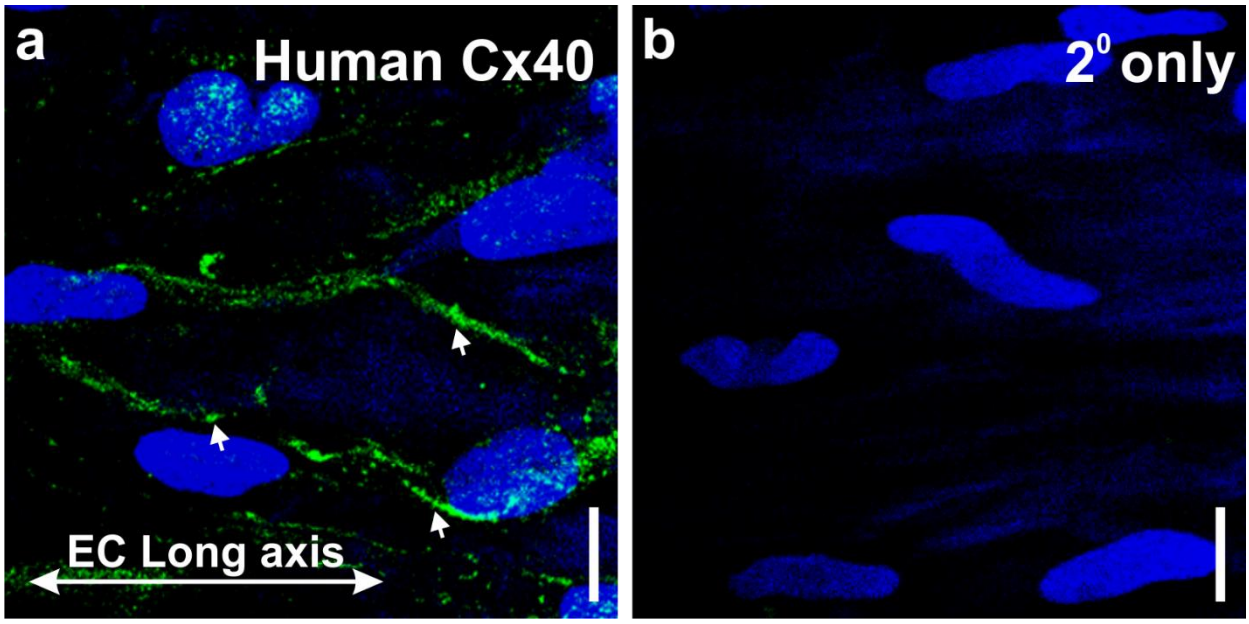

Figure I: Endothelial connexin (Cx) 40 expression in human cerebral arteries. (a) Cx40 (green) was identified in the endothelial layer of human cortical surface artery preparations (en face). Cell nuclei were labeled with DAPI. Arrowheads denote sites on punctate Cx labeling around the periphery of endothelial cells. (b) Absence of Cx40 labeling in tissue treated without primary antibody. Scale bar = 10 µm.

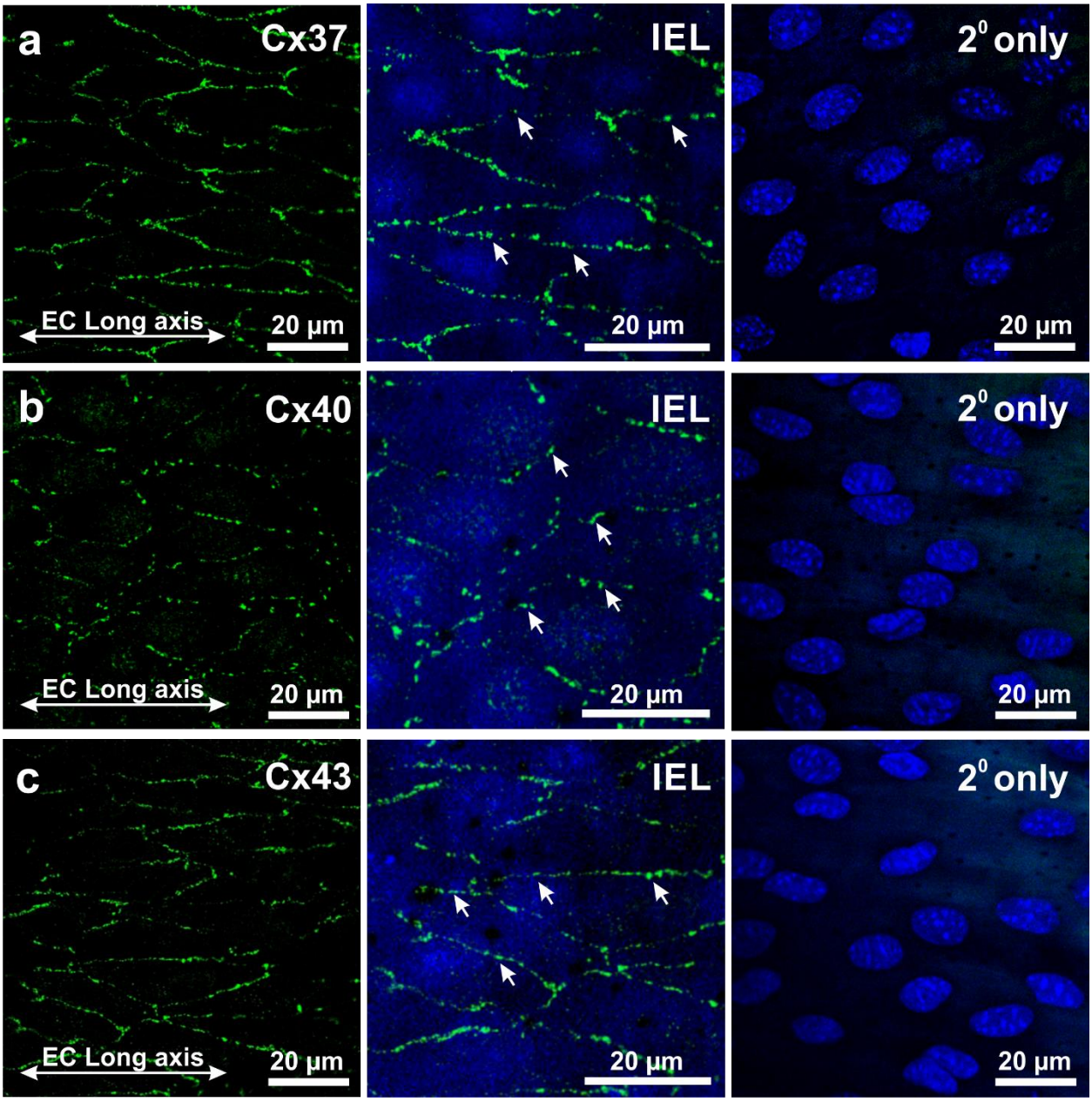

Figure II: Endothelial connexin (Cx) are robustly expressed in cerebral arteries from C57BL/6 mice. (Left) Connexin isoforms Cx37 **(a)**, Cx40 **(b)** and Cx43 **(c)** (green), were identified by immunohistochemistry in the endothelial layer of middle cerebral arteries from C57BL/6 mice. **(Middle)** Arrowheads denote sites on punctate Cx labeling around the periphery of endothelial cells and IEL was delineated by autofluorescence (488 nm). (**Right)** Absence of endothelial Cx labeling in opened arteries incubated without the primary antibody; nuclei were labeled with DAPI. Scale bar = 20 µm.

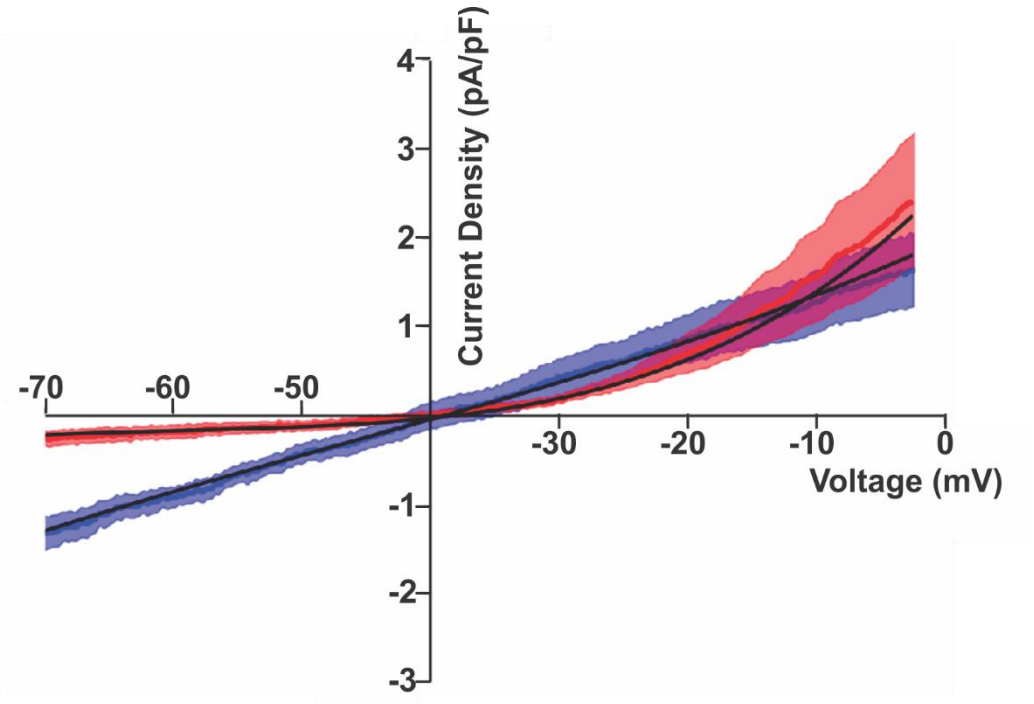

Figure III. Polynomial fits of IV-curves from isolated cerebral arterial cells. Representative whole cell currents from mouse endothelial and smooth muscle cells were collected in physiological bath and pipette solutions (4). Data was fitted with a polynomial curve and values were incorporated into the virtual arterial model to account for ion channel activity. Whole cell capacitance was 8.0 pF and 18.7 pF for the endothelial (blue) and smooth muscle (red) cell, respectively.

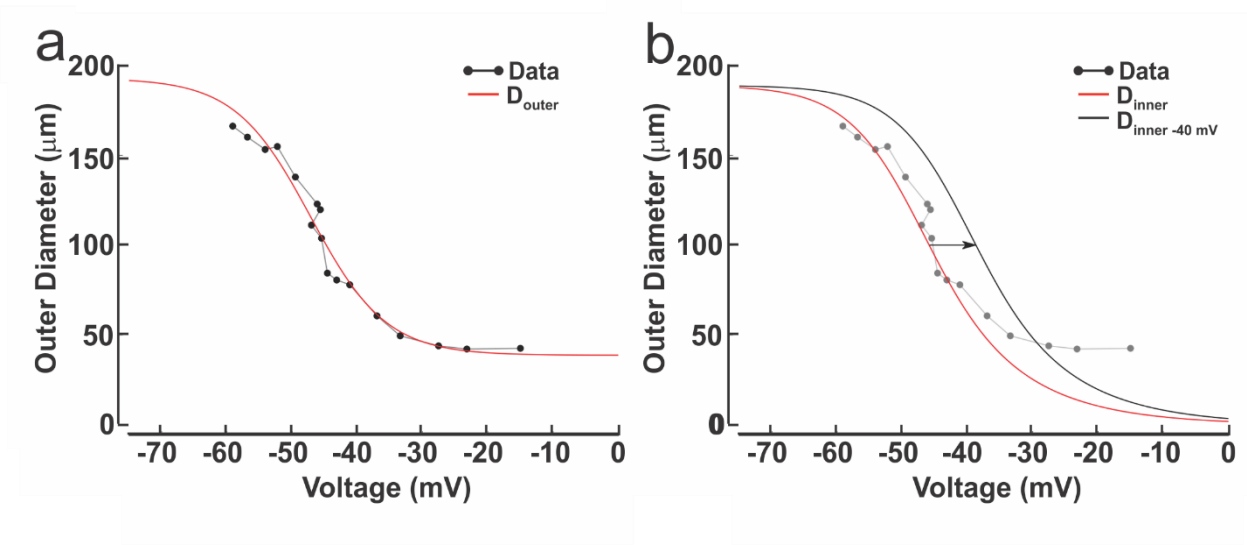

Figure IV. Calculated relationship between diameter and arterial V_m. (a) Data illustrative of the relationship between arterial V_M and outer cerebral arterial diameter was plotted (2) and a sigmoid function (red curve; see Eq.1) applied. **(b)** Inner diameter was represented by assuming that a vessel is fully contracted at 0 mV and that the cross-sectional vessel area is constant across measurements (red curve). This curve was right-shifted to correspond to a resting V_m of −40 mV; black curve). While either inner or outer diameter could be modelled, the latter was chosen to facilitate comparisons with the neurovascular coupling experiments in Fig. 5.

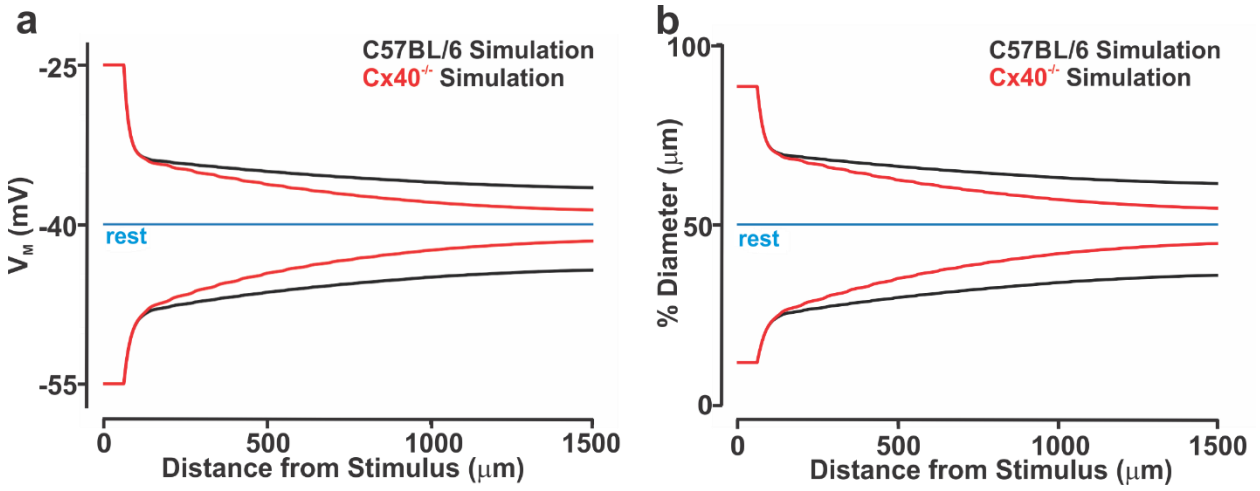

Figure V. *In silico* modeling: Electrical communication in a virtual cerebral artery. A virtual model akin to an isolated cerebral artery (length, 1500μm; diameter, 75 μm; one layer of endothelium and one layer of smooth muscle) was constructed to study electrical communication. **(a, b)** One distal arterial segment was voltage clamped (15 mV negative or positive to resting V_m; 250 ms) and the spreading electrical/vasomotor responses were quantitated along the virtual vessel; endothelial-to-endothelial coupling resistance was set to 1.7 (C57BL/6 control) or 6.0 ($Cx40^{-/-}$) MΩ (calculated in Figure 2). Clamping both cell layers elicits a biphasic response due to 1) a strong but local V_M change in smooth muscle, due to its high compound resistance; and 2) a decidedly lower V_M perturbation in the endothelium as charge readily flows along this cell layer. When translated to diameter, this biphasic response is modestly dampened by the sigmoid shape of the V_M-diameter relationship. Increasing endothelial-to-endothelial coupling resistance ($Cx40^{-/-}$ simulation) enhanced electrical/vasomotor decay relative to control (C57BL/6 simulation).

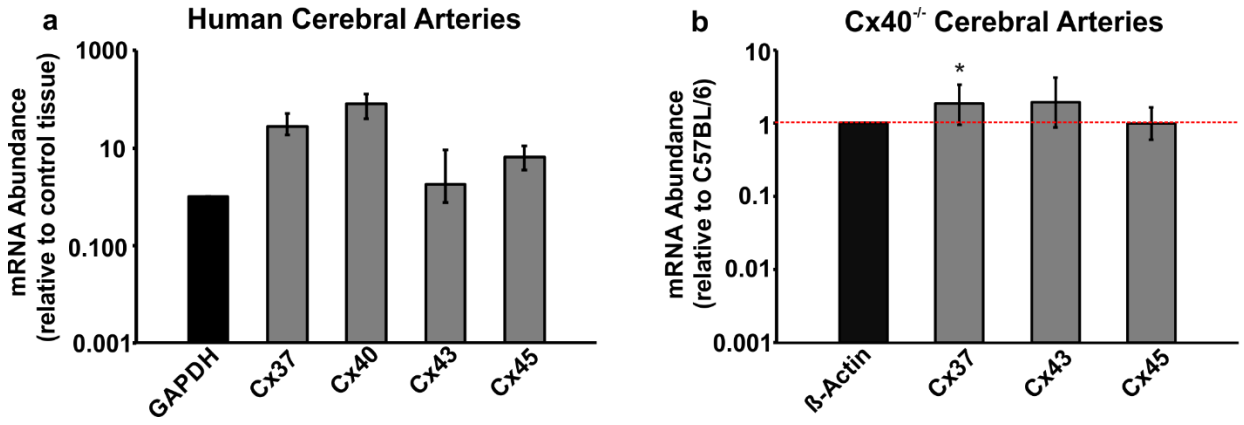

Figure VI. Vascular connexin (Cx) abundance in human and Cx40$^{-/-}$ mice cerebral arteries. **(a)** qPCR analysis revealed the presence of Cx37, Cx40, Cx43 and Cx45 in isolated human cerebral arteries where Cx40 mRNA was observed to be the most abundant. Samples were standardized to reference gene (GAPDH) and were normalized to control tissue (human whole heart RNA). **(b)** A statistically significant increase in Cx37 mRNA was noticed in Cx40$^{-/-}$ mice middle cerebral arteries (MCA), compared to wild type controls (C57BL/6, Cx40$^{+/+}$). Regulation of other connexins were unaffected by the deletion of Cx40 protein. Samples were standardized to reference gene (ß-Actin) and were compared to MCA from C57BL/6 mice. Red dotted line indicates expression in C57BL/6 cerebral arteries. * denotes significant difference.

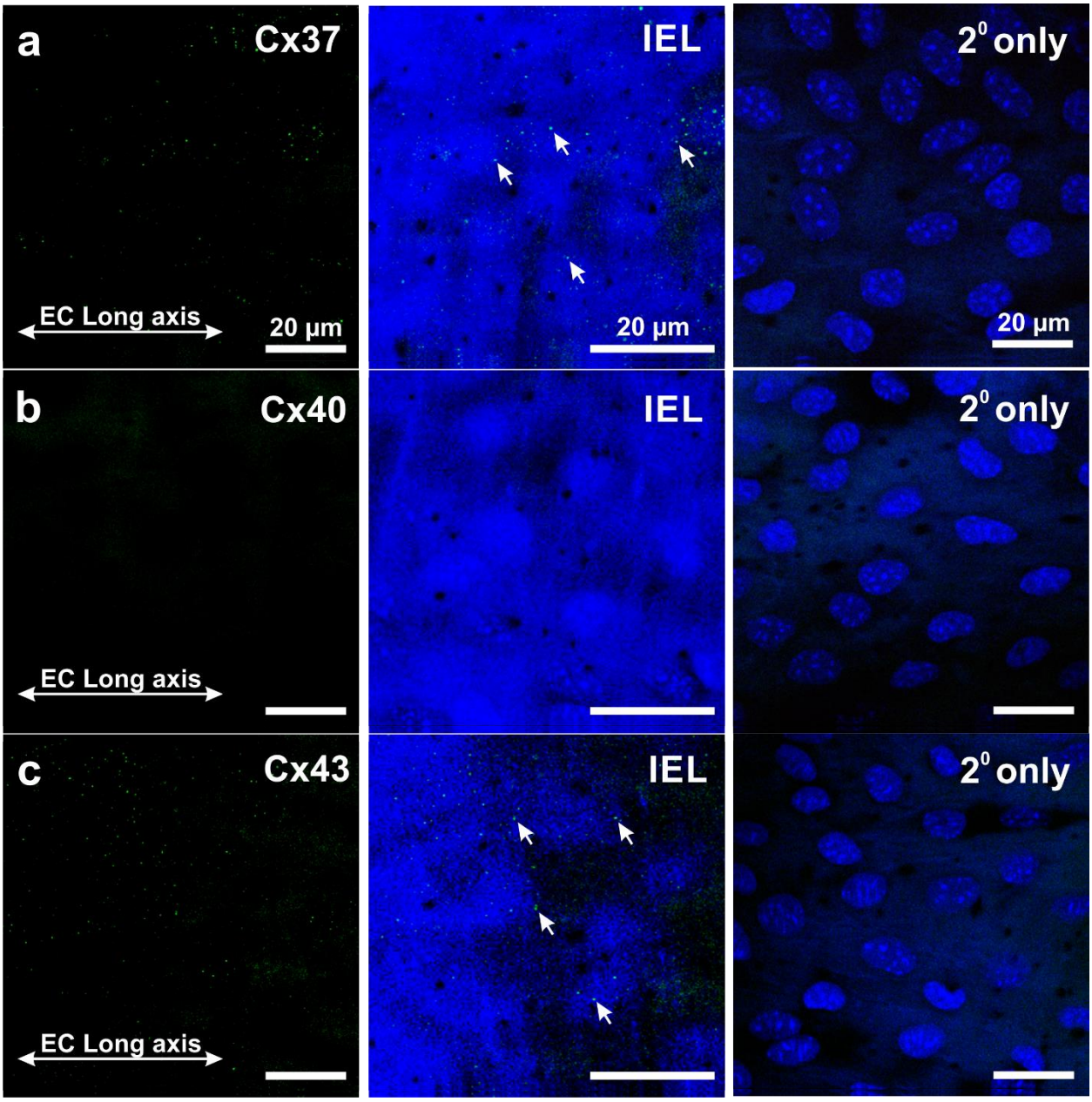

Figure VII: Endothelial connexin (Cx) expression is diminished in cerebral arteries from Cx40$^{-/-}$ mice. **(Left)** Connexin isoforms Cx37 **(a)** and Cx43 **(c)** (green), were identified by immunohistochemistry in the endothelial layer of middle cerebral arteries from Cx40$^{-/-}$ mice. Lack of Cx40 labeling was confirmed in the middle cerebral arteries (**b**). **(Middle)** IEL was delineated by 488 nm autofluorescence and arrowheads denote sites on punctate Cx labeling in the endothelial cell layer. (**Right)** Absence of endothelial Cx labeling in opened arteries incubated without primary antibody; nuclei were labelled with DAPI. Scale bar = 20 µm.

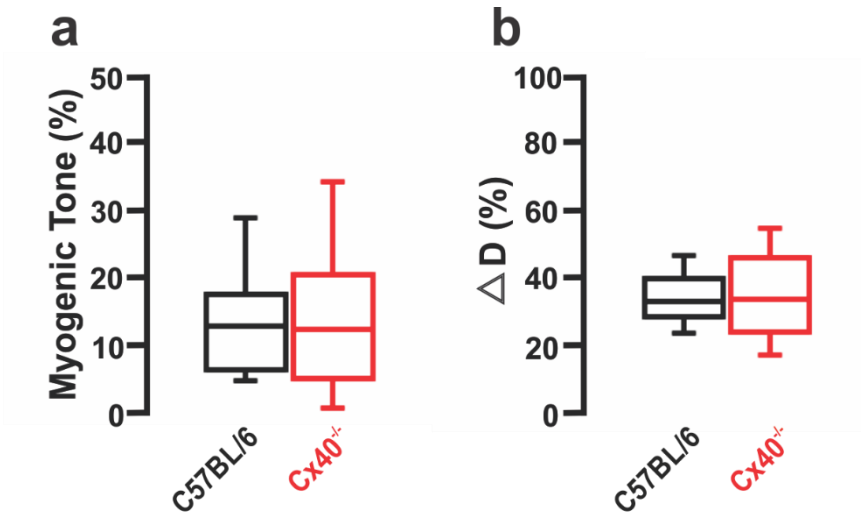

Figure VIII. Cerebral vessel reactivity in C57BL/6 and Cx40$^{-/-}$ mice. Middle cerebral arteries from mice were isolated and pressurized to 50 mmHg. **(a)** Myogenic tone, expressed as a percent of maximal diameter, was similar in cerebral arteries from C57BL/6 and Cx40$^{-/-}$ mice. Maximal diameter was determined by superfusing cerebral arteries in Ca^{2+} free PSS containing 2 mM EGTA. **b)** KCl (60 mM) was superfused in Ca^{2+} PSS and the constriction responses were monitored. Vasomotor measurements expressed as a percent of resting diameter shows no difference between C57BL/6 and Cx40$^{-/-}$ mice.

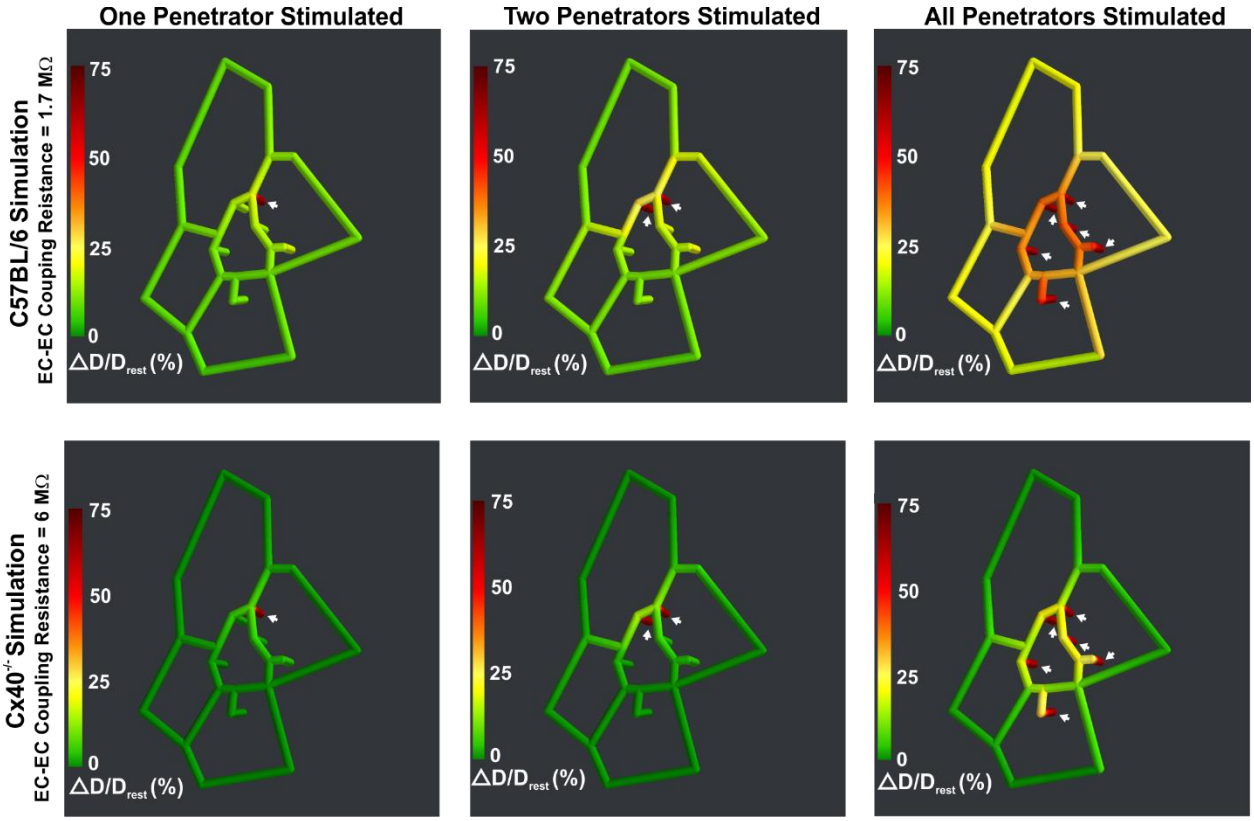

Figure IX. *In silico* modeling: The ascension of vasodilation from penetrating arterioles to surface vessels. Using observations from Shih et al., 2009 (1), a network model of surface arteries and penetrating arterioles was built to study the spread of electrical/vasomotor responses. The *in silico* network consisted of an interconnected network of surface arteries and six adjoining penetrating arterioles. Simulations entailed voltage clamping (15 mV negative to resting V_m, 250 ms) one distal segment in one, two or all penetrating arterioles and resolving the vasomotor response throughout the network. The ascension of vasomotor responses was color mapped along the network; endothelial-to-endothelial coupling resistance was set to 1.7 (C57BL/6 control) or 6 ($Cx40^{-/-}$) MΩ (calculated in Figure 2). Vasomotor responses were expressed relative to resting diameter.

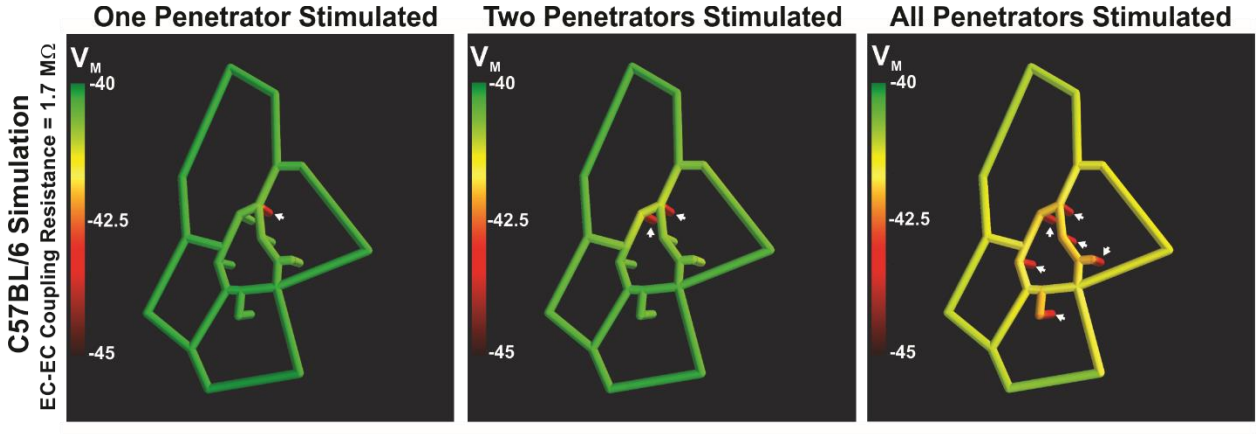

Figure X: Ascension of hyperpolarization from penetrating arterioles to surface vessels is preserved at a lower simulation threshold. Using observations from Shih et al., 2009 (1), a network model of surface arteries and penetrating arterioles was built to study the spread of electrical/vasomotor responses. The *in silico* model consisted of an interconnected network of surface arteries and six adjoining penetrating arterioles. In comparison to Fig. 4, the initial hyperpolarizing response was moderated to 5 mV negative to resting V_m (250 ms). The ascension of electrical responses was color mapped along the network after simulating one, two or all of the penetrators.

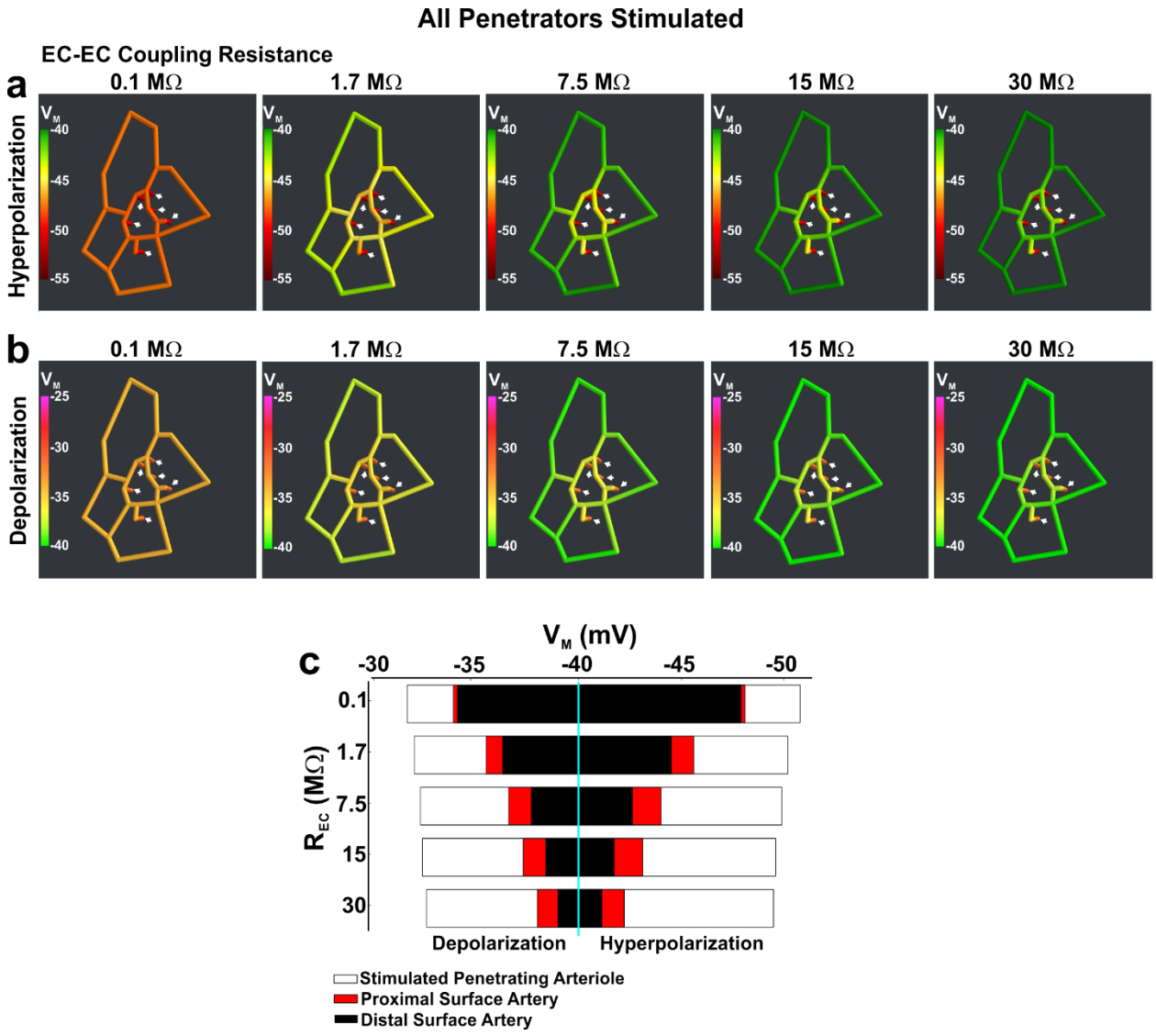

Figure XI. *In silico* modeling: The impact of endothelial-to-endothelial coupling resistance on the ascension of electrical responses from penetrating arterioles to surface vessels. Using observations from Shih et al., 2009 (1), a network model of surface arteries and penetrating arterioles was built to study the spread of electrical responses. The *in silico* model consisted of an interconnected network of surface arteries and six adjoining penetrating arterioles. Simulations entailed voltage clamping (15 mV positive or negative to resting V_m, 250 ms) one distal segment in all penetrating arterioles and resolving the electrical response throughout the network. **(a, b)** The ascension of electrical responses was color mapped along the network after setting the endothelial-to-endothelial coupling resistance at 0.1, 1.7, 7.5, 15 or 30 MΩ. **c)** Summary data was plotted at 3 sites in the network as defined in Figure 3, which included the penetrating arteriole (200 µm upstream from the stimulation site) and two surface vessel sites.

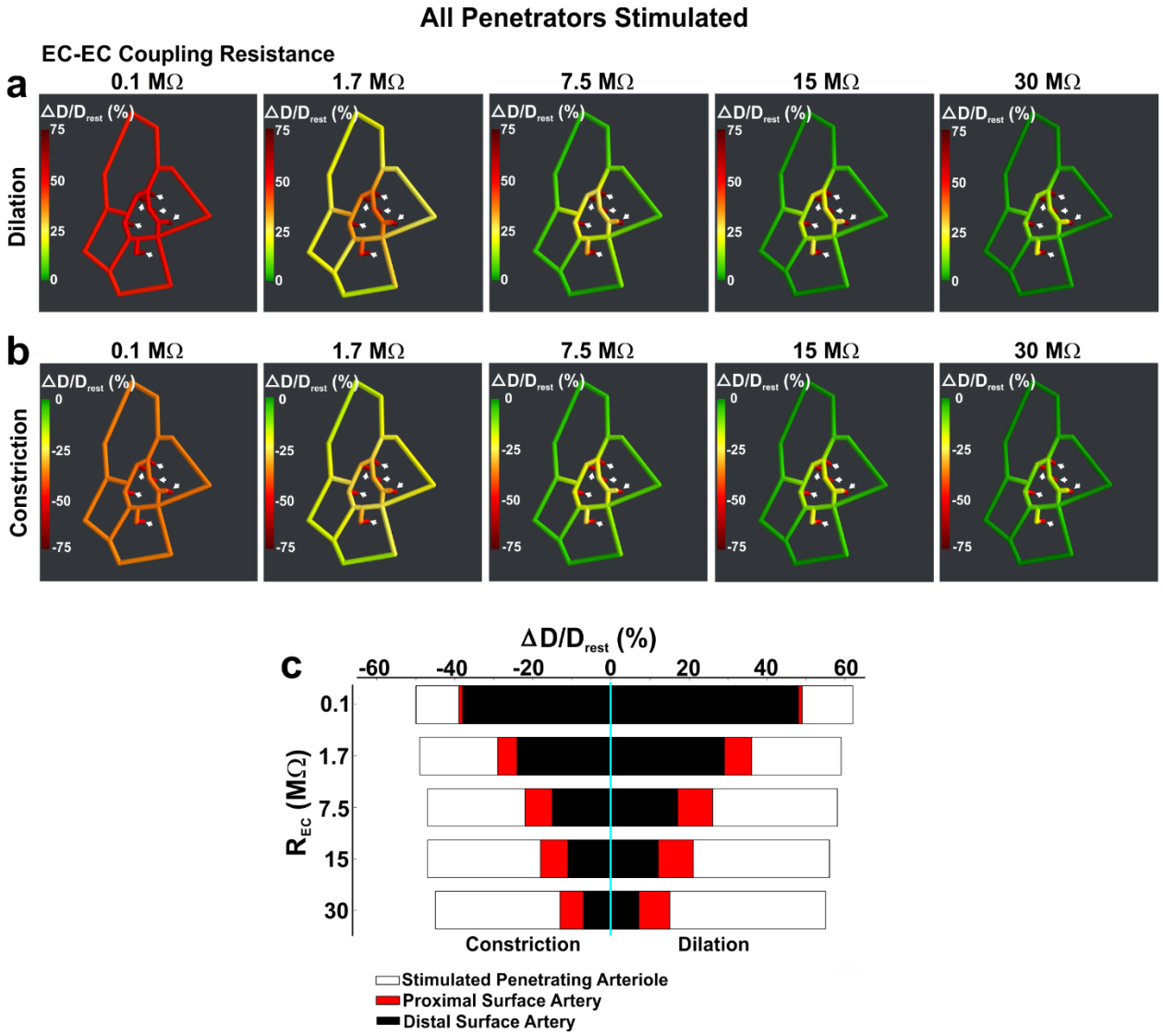

Figure XII. *In silico* modeling: The impact of endothelial-to-endothelial coupling resistance on the ascension of vasomotor responses from penetrating arterioles to surface vessels. Using observations from Shih et al., 2009 (5), a network model of surface arteries and penetrating arterioles was built to study the spread of vasomotor responses. The *in silico* network consisted of an interconnected network of surface arteries and six adjoining penetrating arterioles. Simulations entailed voltage clamping (15 mV positive or negative to resting V_m, 250 ms) one distal segment in all penetrating arterioles and resolving the vasomotor response throughout the network. **(a, b)** The ascension of vasomotor responses was color mapped along the network after setting the endothelial-to-endothelial coupling resistance at 0.1, 1.7, 7.5, 15 or 30 MΩ. **c)** Summary data was plotted at 3 sites in the network as defined in Figure 3, which included the penetrating arteriole (200 µm upstream from the stimulation site) and two surface vessel sites. Vasomotor responses were expressed relative to resting diameter.

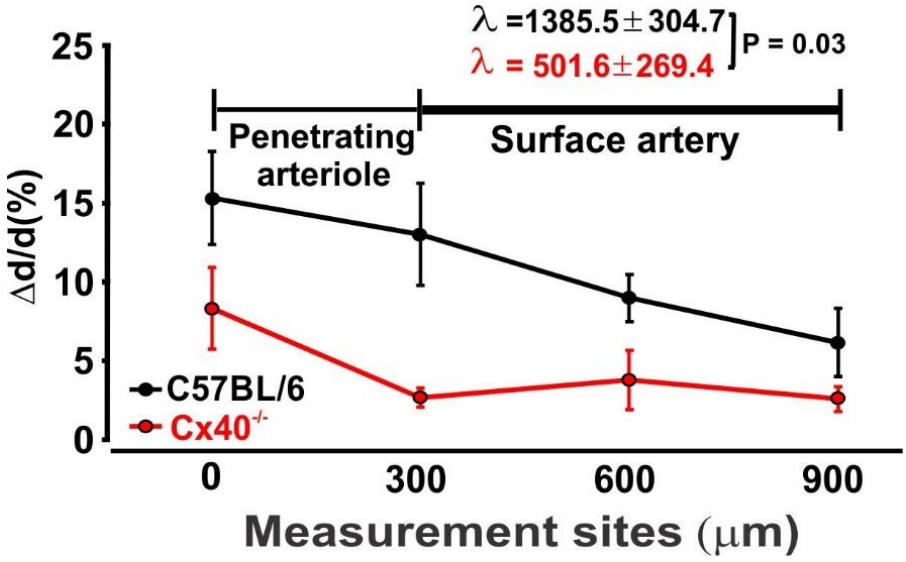

Figure XIII: Compromised vascular signaling impairs conduction of neurovascular coupling responses. Awake mice were positioned on an exercise ball and the FITC Dextran labelled microvasculature was imaged using two-photon microscopy. Starting near a point of barrel cortex activation vasomotor responses to whisker stimulation were monitored at 4 sites upstream sites (spaced 300 µm apart). To assess conduction decay, individual data sets were fitted to an exponential function f(x) = k*exp(-x/lambda), using the nonlinear least-squares Marquardt-Levenberg algorithm. A single tailed- t-test then compared the summative decay constant from C57BL/6 and $Cx40^{-/-}$ mice. $P < 0.05$ denotes significant difference.

Supplemental Tables

Table I: Number of animals/vessels per experiment.

Results in	**Experiment**	**N number.**
Figure 1	Electron Microscopy (C57BL/6J) Immunohistochemistry (C57BL/6J)	(3) (5)
Figure 2	Human cerebral artery Conduction (Endothelium intact) (C57BL/6J) (Cx40$^{-/-}$) Endothelial denuded Conduction (C57BL/6J) (Cx40$^{-/-}$) Membrane potential (C57BL/6J) (Cx40$^{-/-}$)	(450µm, 3; 900µm, 3; 1350µm, 3; 1800µm, 3) (0µm, 7; 450µm, 10; 900µm, 10; 1350µm, 8; 1800µm, 8) (0µm, 7; 450µm, 10; 900µm, 10; 1350µm, 10; 1800µm, 10) (0µm, 7; 450µm, 7; 900µm, 7; 1350µm, 7; 1800µm, 7) (0µm, 7; 450µm, 7; 900µm, 7; 1350µm, 7; 1800µm, 7) (6) (5)
Figure 3	Conducted Dilation Surface Artery Penetrating Arteriole Immunohistochemistry	(Low K^+, 4; ACh, 3) (Low K^+, 4) (4)
Figure 5	Neurovascular Coupling (C57BL/6J) (Cx40$^{-/-}$)	(0µm, 21; 300µm, 21; 600µm, 19; 900µm, 19: 3 animals) (0µm, 14; 300µm, 14; 600µm, 21; 900µm,16: 6 animals)
Figure 6	Sham Controls (C57BL/6J) (Cx40$^{-/-}$) Stroke MRI (C57BL/6J) (Cx40$^{-/-}$)	 (4) (4) (9) (10)
Figure 7	Stroke MRI, ASL & T2W (C57BL/6J) (Cx40$^{-/-}$) Cresyl Violet staining (C57BL/6J) (Cx40$^{-/-}$)	 (9) (9) (9) (8)

Table II: Number of animals/vessels per experiment.

Results in	Experiment	**N Number.** One vessel per animal unless otherwise stated**.**
Supplemental Material Figure 1	Immunohistochemistry (Cx40) Human cerebral arteries	(2)
Supplemental Material Figure 2	Immunohistochemistry Cx37 Cx40 Cx43	 (4) (4) (4)
Supplemental Material Figure 6	qPCR analysis Human cerebral arteries (C57BL/6J) ($Cx40^{-/-}$)	 (6) (6) (7)
Supplemental Material Figure 7	Immunohistochemistry Cx37 Cx40 Cx43	 (4) (4) (4)
Supplemental Material Figure 8	C57BL/6J) ($Cx40^{-/-}$)	(10) (10)
Text	Blood Pressure/Heart Rate (C57BL/6J) ($Cx40^{-/-}$)	 (10) (10)

Table III: Assessment of Metabolic parameters in C57BL/6J and Cx40$^{-/-}$ mice.

Metabolic Parameters	Light/Dark cycle	C57BL/6J	Connexin 40$^{-/-}$
Rate of oxygen consumption	Light	3185.82 ± 215.95	2645.98 ± 255.57
	Dark	3850.68 ± 208.98	3237.83 ± 301.54
Rate of carbon dioxide consumption	Light	3077.83 ± 190.25	2481.76 ± 185.22
	Dark	3864.53 ± 204.20	3203.82 ± 323.64
Respiratory exchange ratio	Light	0.97 ± 0.01	0.94 ± 0.05
	Dark	1.00 ± 0.00	0.99 ± 0.04
Cumulative mass of food consumed	Light	1.46 ± 0.14	1.81 ± 0.72
	Dark	3.00 ± 0.28	2.40 ± 0.72
Cumulative volume of water consumed	Light	1.09 ± 0.14	1.56 ± 0.34
	Dark	3.27 ± 0.19	3.22 ± 0.62
Total number of infrared beam breaks	Light	**311.30 ± 21.95**	**200.75 ± 37.54**
	Dark	**762.66 ± 57.81**	**558.39 ± 92.26**
Number of sleep epochs	Light	412.00 ± 15.06	433.00 ± 19.05
	Dark	217.17 ± 12.12	251.50 ± 26.41
Body weight	-	24.40 ± 1.76	26.32 ± 1.30

Table IV: qPCR-primers utilized for gene expression analysis.

Gene Target	Ascension Number	Primer sequence
Cx37 (GJA4)	NM_008120	GGT CGT CCC CTC TAC CT ACC GTT AAC CAG ATC TTG CC
Cx40 (GJA5)	NM_001271628	GTT TCA ACT TCG ACC TCA CTC T GCT CCA GTC ACC CAT CTT G
Cx43 (GJA1)	NM_010288	CCT TTG ACT TCA GCC TCC AA GAC CTT GTC CAG CAG CTT C
Cx45 (GJC1)	NM_008122	GGT AAC AGG AGT TCT GGT GAA TCG AAA GAC AAT CAG CAC AGT
(β-Actin)	NM_007393	GGC TGT ATT CCC CTC CAT CG CCA GTT GGT AAC AAT GCC ATG T

Major Resource Tables

Table I: Animals

Species/Strain	Vendor or Source	Background Strain	Sex
C57BL/6J	The Jackson Laboratory	C57BL/6J	Male
$Cx40^{-/-}$	Prof. Janis M. Burt (University of Arizona, USA)	C57BL/6J	Male

Table II: Animal breeding

Parents	Species	Vendor or Source	Background Strain	Other Information
Male	C57BL/6J	The Jackson Laboratory	C57BL/6J	
Female	$Cx40^{-/-}$	Prof. Janis M. Burt (University of Arizona, USA)	C57BL/6J	

Table III: Antibodies

Target antigen	Vendor or Source	Catalog #	Working concentration	Lot #
Cx 37: Mouse C-terminus synthetic peptide (Source: Rabbit)	Thermofisher	40-4200	1.25ug/ml	
Cx40: Rat C-terminus, aa 328-340, intracellular (Source: Rabbit)	Alomone	ACC205	4ug/ml	
Cx43: Human/Rat C-terminus, aa 363-382 with N-terminally added lysine (Source: Rabbit)	Sigma	C6219	0.365ug/ml	
Alexa Fluor 488: Anti-rabbit (H+L) Secondary Antibody (Source: Donkey)	Thermofisher	A-21206	2ug/ml	
Anti-rabbit IgG (H+L) HRP: Secondary Antibody, (Source: Goat)	Thermofisher	65-6120	0.1ug/ml	